CFD Modeling of Single-Phase Flow in a Packed Bed with MRI Validation

David J. Robbins, M. Samir El-Bachir, and Lynn F. Gladden
Dept. of Chemical Engineering & Biotechnology, University of Cambridge, Pembroke Street,
Cambridge CB2 3RA, U.K.

R. Stewart Cant
Dept. of Engineering, University of Cambridge, Trumpington Street, Cambridge CB2 1PZ, U.K

Erik von Harbou
Dept. of Mechanical and Process Engineering, University of Kaiserslautern, 67663 Kaiserslautern, Germany

DOI 10.1002/aic.13767

Computational fluid dynamics (CFD) simulations are becoming increasingly widespread with the advent of more powerful computers and more sophisticated software. The aim of these developments is to facilitate more accurate reactor design and optimization methods compared to traditional lumped-parameter models. However, in order for CFD to be a trusted method, it must be validated using experimental data acquired at sufficiently high spatial resolution. This article validates an in-house CFD code by comparison with flow-field data obtained using magnetic resonance imaging (MRI) for a packed bed with a particle-to-column diameter ratio of 2. Flows characterized by inlet Reynolds numbers, based on particle diameter, of 27, 55, 111, and 216 are considered. The code used employs preconditioning to directly solve for pressure in low-velocity flow regimes. Excellent agreement was found between the MRI and CFD data with relative error between the experimentally determined and numerically predicted flow-fields being in the range of 3–9%. © 2012 American Institute of Chemical Engineers *AIChE J,* 58: 3904–3915, 2012

Keywords: computational fluid dynamics, trickle-bed reactor, magnetic resonance imaging, reactor modeling, preconditioning

Introduction

The motivation for this work is to develop and validate computational fluid dynamics (CFD) codes for the prediction of two-phase flow with chemical reaction in packed-bed reactors or, as they are more commonly called, trickle-bed reactors. As a first step in achieving this, we report the implementation of a CFD code for the prediction of single-phase flow in a packed bed and the quantitative comparison of the CFD prediction with velocity fields within the bed recorded using magnetic resonance imaging (MRI). Several validation studies of single-phase simulations have been previously reported in the literature. The purpose of the validation presented in this article is to demonstrate that an explicit density-based solver (used here in preference to the more common implicit pressure-based approach) can simulate low-speed flow with adequate accuracy. To this end, simulation results will be compared to highly spatially resolved velocity maps obtained from MRI experiments.

Trickle-bed reactors are broadly defined as reactors in which the liquid and gas phases flow cocurrently downward through a packed bed. They are the most frequently used type of gas–liquid–solid reactor and are used in a wide range of applications in the chemical and biochemical processing industries.[1] Examples of applications of trickle-bed reactors include oxidation and hydrogenation reactions, hydrocracking, hydrodenitrogenation, and wastewater treatment.[2,3]

Trickle-bed reactors can be operated in a range of flow regimes depending on the fluid properties, flow rates and reactor characteristics. The regimes are typically divided into two groups based on the interaction of the liquid and gas flows and the subsequent impact on the flow pattern. The low gas and liquid velocities associated with trickle flow comprise the low-interaction regime, where the flow of one phase is not affected by the flow of the second phase. Increasing the gas and liquid velocities yields greater interactions between the two phases impacting the flow pattern, giving rise to the so-called high-interaction regimes (including pulsing, bubble, and spray flow).[4–7]

Many industrial trickle-bed reactors are operated either in trickle or pulsing flow or in a region near to the transition regime, and thus, understanding the nature and characteristics of the hydrodynamics of these regimes has been a subject of long-standing interest.[6,8–12] Although physically simple, trickle-bed reactors are inherently difficult to model numerically due to the coupling of reaction kinetics, mass transfer, global- and local-scale hydrodynamics, and two-phase interaction.[13] This complexity has a direct impact on

---

Correspondence concerning this article should be addressed to L. F. Gladden at lfg1@cam.ac.uk.

computational modeling and scale-up methods, which often rely on correlations and nonvalidated codes to predict the internal hydrodynamics and mass transfer. Prevalent hydrodynamical phenomena of interest inside trickle-bed reactors include two-phase flow, flow transition, capillary action, liquid dispersion as a result of a changing porosity profile and flow hysteresis, and maldistribution.

CFD studies

CFD is a powerful tool for modeling fluid flow in chemical reactors. CFD is becoming increasingly widespread with the advent of mainstream multicore processors in addition to the increased processing power of the cores themselves. In consequence, CFD has been applied to a variety of areas including turbomachinery,[14,15] aerospace flows,[16] and weather modeling.[17]

In a chemical engineering context, CFD is used to aid reactor design, optimize usage and diagnose faulty operation within existing reactors. In this context, CFD simulations can be broadly categorized into two approaches: the porosity-distributed resistance (PDR) approach whereby the porosity is implicitly included in the geometry via the generation of a radial porosity distribution superimposed on an empty domain, and high-fidelity simulations in which all the internal components of the reactor are individually modeled. The work presented in this article is based on the latter simulation procedure.

Gunjal et al.[18] used a CFD code validated with MRI data recorded by Suekane et al.[19] to determine the effect of the single-phase flow structure and packing on heat transfer and surface stress in a packed-bed reactor; this is an example of a high-fidelity simulation. The CFD code (FLUENT) was validated using a one-dimensional (1-D) slice of the highest Reynolds-number data through a slice in the geometry with the highest cross-sectional area. The highest Reynolds number was chosen due to the low scatter in the reported experimental data compared with the other experimental results. In subsequent computations, it was assumed that the validated code would maintain the same level of accuracy for flows with lower Reynolds numbers and in other regions of the geometry with narrow parts and contact points. The assumption that the validation holds for lower Reynolds numbers and through areas of the reactor with lower cross-sectional areas has yet to be fully demonstrated in the literature. In the work of Gunjal et al.,[18] the pressure field was determined using the SIMPLE algorithm based on the correction of a guessed pressure field to satisfy the continuity equation. This requires the solution of a Poisson equation for the pressure correction, which loses convergence effectiveness as the mesh is refined to achieve a higher spatial accuracy. An alternative approach is to use preconditioning methods within a density-based solver, which is the method used in this work. This approach is taken because we wish to produce high-fidelity simulations for low-velocity flows at high spatial resolution with high accuracy; such simulations will be computationally expensive. Using a density-based solver, we not only avoid the use of a Poisson solver but also develop a code which is easily parallelized, as the algorithm is fully explicit. We use the preconditioning method[20] to extend the validity of the density-based approach to the low flow velocities typical of trickle-bed reactors.

Two-phase flow simulations have been investigated by a number of groups,[13,21–25] demonstrating the need to implement the inertial, gravitational, viscous, and capillary forces in the momentum balance used in the computation to investigate the hydrodynamics of the trickle-flow regime. Dixon and Nijemeisland[26] used a high-fidelity simulation to predict radial temperature profiles in packed-bed reactors and concluded that CFD analysis had the potential to generate a large amount of pertinent data for use in 3-D heterogeneous models or closure relationships. Subsequent work provided insight into the near-wall effect and wall hot-spot formation caused by local catalyst deactivation and asymmetric temperature profiles across the catalyst particles.[27,28] We note for completeness that the work of Dixon and Nijemeisland[26] addressed higher particle Reynolds numbers than are considered in the work to be presented here.

Jiang et al.[21] have also addressed a wide range of issues related to CFD studies of trickle-bed reactors by application of the PDR class of simulations. Three different models for the particle–fluid exchange coefficients for closure of the capillary pressure terms were investigated; the stochastic nature of the exact 3-D interstitial void structure was cited as one of the principal challenges of modeling a trickle-bed reactor. It was also noted that there is no overall governing force in a trickle-bed reactor, with contributions from the capillary, gravitational, viscous, and inertial forces of approximately the same order of magnitude. Later work incorporating the mixing-cell network model with CFD showed heterogeneity of the liquid reactant within a trickle-bed reactor even with a uniform inlet flow condition, with high concentrations in zones of high porosity. Such effects would have a direct impact on the concentration of reactant available at the catalyst surface, and thus, the effectiveness of the trickle-bed reactor.[22]

High-fidelity CFD studies by Lopes and Quinta-Ferreira[23] have highlighted the influence of local-scale interstitial phenomena in trickle beds on the utilization of the catalyst bed and liquid flow maldistribution. The impact of operating pressure on the liquid holdup profile within the reactor was also investigated, with increasing operating pressure found to smooth the radial profiles for liquid and gas holdup. More recently, Lappalainen et al.[24] used PDR-based CFD to investigate liquid dispersion via the mechanical, capillary, and overloading mechanisms, showing that mechanical dispersion is dominant for larger particles and that capillary dispersion is dominant for smaller particles. It was noted that the effect of imposing a random Gaussian fluctuation on the radial porosity profile served to generate minor dispersive flow behavior when separate models for dispersion were not included; however, this behavior became irrelevant when capillary and mechanical dispersion were explicitly modeled. This implies that imposing a random Gaussian fluctuation on the radial porosity profile in a PDR-style simulation appears to recapture some of the physics that has been lost by not explicitly modeling the effects of dispersion in the balance equations.

It is generally recognized that CFD codes should be fully validated with experimental data in order for the computational results to be accepted and usable in reactor design and optimization. Codes such as FLUENT and CFDLib have been validated[21,25] by comparing global hydrodynamic parameters such as bed pressure drop and liquid holdup to experimental data as well as measurements of liquid velocity at low spatial resolution. Such approaches do not consider whether or not the simulation is accurately reproducing the true internal flow structures and the extent of local hydrodynamic variation in the flow field. In this article, MRI data are used as a means to validate the local hydrodynamics of single-phase flow in a packed bed computed by an in-house CFD code. Given that the literature has demonstrated that CFD simulations are in agreement with global hydrodynamic parameters,[18,25] it is essential that the simulations are also shown to accurately predict the local flow fields both qualitatively and quantitatively. Once the single-phase nonreactive flow has been validated, further studies can be initiated to validate the code for two-phase reactive flow. MRI is an ideal tool for validating CFD results owing to its ability to noninvasively resolve important hydrodynamic quantities such as flow fields, holdup, wetting efficiency, and porosity at high spatial resolution.[29–31]

The structure of this article is first to present, briefly, the MRI method used to acquire the data, followed by the presentation of the computational method to discretize the fluxes and solve the Navier–Stokes equations using a density-based solver. It is an aim of the article to predict low Reynolds number flows assumed as incompressible, as these flow fields are important in determining the heat and mass transfer performances of packed-bed reactors. Particular focus will, therefore, be given to the preconditioning method used to solve the incompressible Navier–Stokes equations, which uses a compressible time-marching algorithm and couples the velocity and pressure fields together without the need for a further numerical method for solution of the Poisson equation for pressure. Simulation results for four cases will be presented as 2-D contour plots of Reynolds number as a qualitative indication of the flow fields within the packed bed, followed by a quantitative comparison of the experimental and computational flow fields by examining distribution functions and 1-D velocity plots across four chosen regions of the geometry.

Experimental and Computational Methods

MRI measurements

A schematic of the packed bed is shown in Figure 1, indicating how the image slice is oriented with respect to the bed. The packed bed used in the MRI experiments was a column of inner diameter 38.0 ± 0.1 mm packed with plastic spheres of diameter 19 mm spheres in a structured formation; each layer was rotated by 90° with respect to the layer immediately above or below it.[33] The flow through the bed was induced using a pressure head differential between two reservoirs. Two-dimensional images of the flow through the bed were taken in an image slice perpendicular to the direction of superficial flow, through layer 33 of the packing; previously images had been acquired to confirm that the flow had fully developed at this position within the bed and that the flow images were, therefore, free from entrance/exit affects. All experiments were carried out on a Bruker Spectrospin DMX200 14.9 cm bore spectrometer using a birdcage coil of length and diameter 6.4 cm, operating at a proton (^{1}H) resonance frequency of 199.7 MHz. The bed was positioned within the vertical bore of a 4.7 T superconducting magnet. The velocimetry data were recorded using a standard spin-echo phase-encoding velocity measurement pulse sequence,[29] in which the velocity is quantified by the phase shift induced by successive increments of the velocity encoding gradients. Images were obtained at four different inlet particle Reynolds numbers for water (Re_p): 27, 55, 111, and 216. The particle Reynolds number (Re_p) is defined as

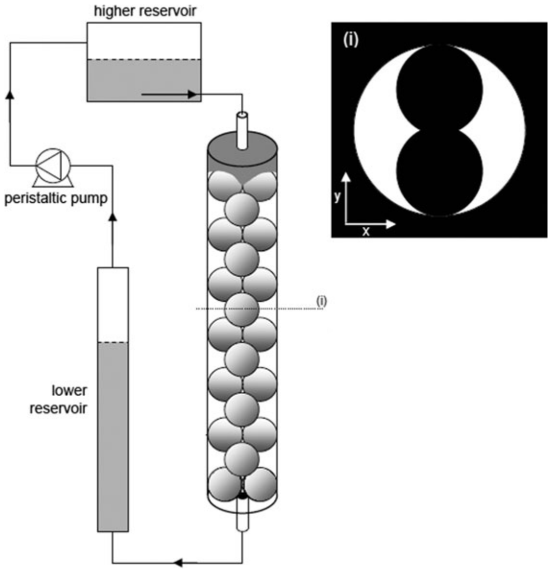

Figure 1. Schematic of experimental set-up for acquisition of MRI data.

The dashed line (i) identifies a representative 2-D image slice recorded through a layer of the bed, typical of that used in this study. Figure reproduced from Sains.[32]

$$Re_\mathrm{p} = \frac{\rho u d_\mathrm{p}}{\mu} \tag{1}$$

where d_p is the particle diameter.

The duration of the velocity encoding gradients was 2 ms (1 ms for the case of $Re_\mathrm{p} = 216$) and the observation time was 20 ms (11 ms for the case of $Re_\mathrm{p} = 216$). Four velocity encoding gradients of 3.00, 1.50, 0.75, and 0.625 G/cm were used corresponding to the cases of $Re_\mathrm{p} = 27$, 55, 111, and 216, respectively. The acquired images have an in-plane resolution of 0.195 × 0.195 mm^2 and a transverse slice thickness of 1 mm. The total acquisition time for a single image was 20 min.

We note that the geometry chosen, and hence flow field observed, is more complex than that studied by Suekane et al.[19]; this results in a more complex evolution of the flow field due to inertial effects, as a function of Reynolds number, than will be observed in the simpler packing geometry. The MRI data used in this work, therefore, provide a greater test of the capability of the CFD simulation to predict the high spatial resolution structure of a flow field across a range of Reynolds numbers. In particular, Suekane at al. studied the development of inertial flow structures in a packed bed of five unit cells packed as a simple cubic lattice. Each of the six layers contained four 1/4-spheres of diameter 28 mm, packed within a cylinder of internal diameter 46 mm. Within this packing the main body of the flow is through a central region of void space containing relatively fast moving liquid.

CFD

The CFD code "Navier-Stokes and Euler with Tetrahedra" (NEWT) is a 3-D unstructured, finite-volume method code developed at the Department of Engineering at the University of Cambridge.[34] It was originally designed for simulation of turbomachinery and other complex flows of interest and in consequence models the compressible flow of ideal gases. NEWT is used as the foundation code for this investigation due to its good stability and convergence characteristics and the ability to access and edit the source code, which is written in FORTRAN.

In the low-subsonic flow regime associated with trickle-bed reactors, the velocity magnitude of the flow becomes small in comparison to the speed of sound. This reduces the computational efficiency and decreases the rate of convergence of the solution.[35] In this regime, the flow is often assumed to be incompressible; this decouples the solution of pressure from velocity, and thus, a pressure-based scheme such as SIMPLE or an artificial compressibility method[36] is often applied. Nevertheless, there are cases where the flow can change density even at low Mach numbers. In a trickle-bed reactor, strongly exothermic and endothermic surface reactions can cause density gradients as a result of temperature gradients. In such cases, the flow is no longer fully incompressible and the choice of solution method is less clear.[37] It is, therefore, advantageous to implement a code which makes no prior assumptions as to the compressibility of the flow, and this approach will be adopted here.

In this article, the Navier–Stokes equations have been preconditioned to be able to solve both the compressible and incompressible governing equations over the range of subsonic and supersonic flow. Preconditioning focuses on the principle that, for low Mach number flows, the primitive variables (p,u,v,w,T) are of greater importance than the conservative variables $(\rho,\rho u,\rho v,\rho w,\rho E)$.[20] A preconditioning matrix is used to solve the conservation equations for the primitive variables and to ensure stability and convergence at low Mach numbers. This facilitates full coupling of the pressure, accounts for density fluctuations at low Mach numbers, and enables a solution method applicable at all Mach numbers.[38]

The following sections will present the governing equations and the discretization methods used in NEWT.

Governing equations

For the purposes of this study, the single-phase flow is considered nonreactive and isothermal. As such, the energy equation is not considered in the simulations. The Navier–Stokes equations in integral-vector form are

$$\frac{\partial}{\partial t}\int_{\Omega} \boldsymbol{W}\, d\Omega + \oint_{\partial\Omega} (\boldsymbol{F}_{\mathrm{c}} - \boldsymbol{F}_{\mathrm{v}})dS = \int_{\Omega} \boldsymbol{Q}\, d\Omega \tag{2}$$

where $\boldsymbol{W}$, $\boldsymbol{F}_{\mathrm{c}}$, $\boldsymbol{F}_{\mathrm{v}}$, and $\boldsymbol{Q}$ are the vectors of the conservative variables, convective flux, viscous flux, and source terms, respectively. For this study, these vectors are

$$\boldsymbol{W} = \begin{pmatrix} \rho \\ \rho u \\ \rho v \\ \rho w \end{pmatrix}, \boldsymbol{F}_{\mathrm{c}} = \begin{pmatrix} \rho V \\ \rho u V + n_x p \\ \rho v V + n_y p \\ \rho w V + n_z p \end{pmatrix},$$
$$\boldsymbol{F}_{\mathrm{v}} = \begin{pmatrix} 0 \\ n_x\tau_{xx} + n_y\tau_{xy} + n_z\tau_{xz} \\ n_x\tau_{yx} + n_y\tau_{yy} + n_z\tau_{yz} \\ n_x\tau_{zx} + n_y\tau_{zy} + n_z\tau_{zz} \end{pmatrix}, \quad \boldsymbol{Q} = \begin{pmatrix} 0 \\ \rho f_{e,x} \\ \rho f_{e,y} \\ \rho f_{e,z} \end{pmatrix} \tag{3}$$

Preconditioning of the Navier–Stokes equations involves solving for the primitive variables $(\boldsymbol{W}_{\mathrm{p}})$ in the first integral of Eq. (2), and multiplication of the whole equation by a transformation matrix $\boldsymbol{K}$

$$\boldsymbol{K}\frac{\partial \boldsymbol{W}}{\partial \boldsymbol{W}_{\mathrm{p}}}\frac{\partial}{\partial t}\int_{\Omega} \boldsymbol{W}_{\mathrm{p}}\, d\Omega + \boldsymbol{K}\oint_{\partial\Omega} (\boldsymbol{F}_{\mathrm{c}} - \boldsymbol{F}_{\mathrm{v}})dS = \boldsymbol{K}\int_{\Omega} \boldsymbol{Q}\, d\Omega \tag{4}$$

with the primitive variable vector defined as

$$\boldsymbol{W}_{\mathrm{p}} = \begin{pmatrix} p \\ u \\ v \\ w \end{pmatrix} \tag{5}$$

The product of the first element of the transformation matrix $\boldsymbol{K}_{1,1}$ and the first element of the conservative variable Jacobian matrix $\left(\frac{\partial \boldsymbol{W}}{\partial \boldsymbol{W}_{\mathrm{p}}}\right)_{1,1}$ is $\partial\rho/\partial p$. This differential controls the propagation speed of acoustic waves in the solution. Replacing this element with a preconditioning parameter θ facilitates control of the wave propagation speed, allowing the numerical solution to be stabilized. This yields the nonconservative preconditioning matrix, $\boldsymbol{\Gamma}_{\mathrm{nc}}$. The parameter θ can, thus, be regarded as an artificial compressibility coefficient, allowing the compressible equations to be solved for an incompressible flow using the same numerical method via the addition of a time derivative to the continuity equation.[38] For an incompressible flow, θ is defined as

$$\theta = \frac{1}{U_{\mathrm{r}}^2} \tag{6}$$

where U_{r} is a reference velocity defined for incompressible flows by

$$U_{\mathrm{r}} = \max\left(\|\boldsymbol{v}\|, \frac{\upsilon}{\Delta h}, \frac{\kappa}{\Delta h}, \varepsilon\sqrt{\frac{\|\Delta p\|}{p}}, \varepsilon V_{\max}\right) \tag{7}$$

where ε is an arbitrary small number (10^{-3} in NEWT) chosen to prevent the reference velocity becoming zero, υ is the kinematic viscosity of the fluid, κ is the thermal diffusivity, and Δh is a measure of the cell size. The choice of this reference velocity ensures that the solution eigenvalues are all of the same order of magnitude and that the preconditioned equations approach the original Navier–Stokes equations as the Mach number increases to unity.[20] The final set of preconditioned equations is determined by substituting $\boldsymbol{\Gamma}_{\mathrm{nc}}$ into the transformed Eq. 4 and premultiplying by the inverse of the transformation matrix, $\bar{\boldsymbol{K}}^{-1}$

$$\boldsymbol{\Gamma}\frac{\partial}{\partial t}\int_{\Omega} \boldsymbol{W}_{\mathrm{p}}\, d\Omega + \oint_{\partial\Omega} (\boldsymbol{F}_{\mathrm{c}} - \boldsymbol{F}_{\mathrm{v}})dS = \int_{\Omega} \boldsymbol{Q}\, d\Omega \tag{8}$$

$\boldsymbol{\Gamma}$ is the preconditioning matrix, defined for an incompressible system with no energy equation as

$$\boldsymbol{\Gamma} = \left(\boldsymbol{K}^{-1}\boldsymbol{\Gamma}_{\mathrm{nc}}\right) = \begin{pmatrix} \theta & 0 & 0 & 0 \\ \theta u & \rho & 0 & 0 \\ \theta v & 0 & \rho & 0 \\ \theta w & 0 & 0 & \rho \end{pmatrix} \tag{9}$$

In NEWT, preconditioning has been implemented to solve for an incompressible fluid (with θ and U_{r} shown above), an ideal gas or a real fluid. In this study, the simulation is run for the case of an incompressible fluid as only a single-phase liquid flow is considered.

Discretization methods

Temporal Discretization. The method of lines is used to construct the solution equations with time derivatives on the left hand side, and all other terms summed on the right hand side. After rearranging Eq. 8 and spatially discretizing the righthand side, the partial differential equations become an ordinary differential equation of the form

$$\boldsymbol{\Gamma}\Omega_{\mathrm{SC,k}}\frac{\boldsymbol{\delta W}_{\mathrm{p}}}{\boldsymbol{\delta\upsilon}} = \boldsymbol{R}_{\mathrm{c,k}} + \boldsymbol{R}_{\mathrm{v,k}} + \boldsymbol{R}_{\mathrm{s,k}} + \boldsymbol{R}_{\mathrm{AD,k}} = \boldsymbol{R}_{\mathrm{tot,k}} \tag{10}$$

where $\boldsymbol{R}_{\mathrm{tot,k}}$ is the sum of the residuals of the convective and viscous fluxes, the source terms and the artificial dissipation at node k. This is solved in NEWT using a Runge–Kutta time marching algorithm, which in preconditioned form for m stages is

$$\boldsymbol{W}_{\mathrm{p}}{}^{(0)} = \boldsymbol{W}_{\mathrm{p}}{}^{(n)} \tag{11}$$

$$\boldsymbol{W}_{\mathrm{p}}{}^{(m)} = \boldsymbol{W}_{\mathrm{p}}{}^{(m-1)} + \alpha_{\mathrm{m}}\frac{\Delta t}{\Omega_{\mathrm{SC,k}}}\left[\boldsymbol{\Gamma}^{-1}\left(\boldsymbol{R}_{\mathrm{c,k}} + \boldsymbol{R}_{\mathrm{v,k}} + \boldsymbol{R}_{\mathrm{s,k}}\right) + \boldsymbol{R}_{\mathrm{AD,k,prc}}\right] \tag{12}$$

where $\Omega_{\mathrm{SC,k}}$ is the volume of the supercell at node k—the total volume of all cells with node k in common. The stage coefficients α_{m} can be tuned based on the order of accuracy required. The stage coefficients used in NEWT are α_{m} = 0.0833, 0.2069, 0.4265, and 1.0000 for m = 1–4. The time step, Δt, is determined by

$$\Delta t = \sigma f_t \frac{\rho(\Delta h)^2}{(|V'| + c')\rho\Delta h + C\min\left(\mu, \frac{\mu}{\mathrm{Pr}}\right)} \tag{13}$$

where σ is the Courant number, Δh is a measure of the cell size (in this case, the cube root of the supercell volume), f_t is a time step factor allowing for control of the solution progress and V' and c' are the modified contravariant velocity and speed of sound for a preconditioned incompressible flow

$$|V'| = \frac{|\boldsymbol{v}\cdot\boldsymbol{n}|}{2} \tag{14}$$

$$c' = \sqrt{\frac{(\boldsymbol{v}\cdot\boldsymbol{n})^2}{4} + U_{\mathrm{r}}^2} \tag{15}$$

Finally, the inverse preconditioning matrix for an incompressible flow with no energy equation is

$$\underline{\Gamma}^{-1} = \begin{pmatrix} 1/\theta & 0 & 0 & 0 \\ -u/\rho & 1/\rho & 0 & 0 \\ -v/\rho & 0 & 1/\rho & 0 \\ -w/\rho & 0 & 0 & 1/\rho \end{pmatrix} \tag{16}$$

Residual smoothing is used to facilitate a larger time step and to accelerate the progress of the solution.[39] The linear equations are solved using the Jacobi method[34]

$$\boldsymbol{R}_{\mathrm{k}}^{*(m+1)} = \frac{\boldsymbol{R}_{\mathrm{k}} + \varepsilon_{\mathrm{r}}\sum_{l\neq\mathrm{k}}\boldsymbol{R}_{\mathrm{l}}^{*(m)}}{1 + N_{\mathrm{k}}\varepsilon_{\mathrm{r}}} \tag{17}$$

where m is the iteration count, N_{k} are the number of neighbors of node k, l is the notation for a neighboring node, and $\boldsymbol{R}^*$ represents a smoothed residual.

The discretization methods used to calculate the residuals in Eq. 12 are now described.

Convective Flux Discretization. A cell-vertex based scheme is one in which the values of the solution variables are stored at the vertices of the tetrahedral elements. The convective flux is discretized by the summation of the fluxes over the four faces (i) of the tetrahedral cell

$$\oint_{\partial\Omega_j}\boldsymbol{F}_{\mathrm{c}}\,dS = \sum_{i=1}^{4}\overline{\boldsymbol{F}}_{\mathrm{c},i} \tag{18}$$

with the face-averaged flux vector $\overline{F}_{\mathrm{c},i}$ given by

$$\overline{\boldsymbol{F}}_{\mathrm{c},i} = \begin{pmatrix} \overline{\rho V}_{\mathrm{FA},i} \\ \overline{\rho V}_{\mathrm{FA},i}\ \overline{u}_{\mathrm{FA},i} + n_{x,i}\ \overline{p}_{\mathrm{FA},i} \\ \overline{\rho V}_{\mathrm{FA},i}\ \overline{v}_{\mathrm{FA},i} + n_{y,i}\ \overline{p}_{\mathrm{FA},i} \\ \overline{\rho V}_{\mathrm{FA},i}\ \overline{w}_{\mathrm{FA},i} + n_{z,i}\ \overline{p}_{\mathrm{FA},i} \end{pmatrix} \tag{19}$$

where $\overline{\phi}_{\mathrm{FA},i}$ denotes a face-averaged variable for a flow quantity ϕ, and the product of the density and the contravariant velocity is approximated by

$$\overline{\rho V}_{\mathrm{FA},i} \approx n_{x,i}\overline{\rho u}_{\mathrm{FA},i} + n_{y,i}\overline{\rho v}_{\mathrm{FA},i} + n_{z,i}\overline{\rho w}_{\mathrm{FA},i} \tag{20}$$

Each vertex has several cells in common from which it will obtain a value for the convective flux. The nonweighted sum method[40] is implemented to calculate the nodal convective flux residual

$$\boldsymbol{R}_{\mathrm{c,k}} = \sum_{j=1}^{N_{\mathrm{k}}}\boldsymbol{R}_{\mathrm{c,J}} = \sum_{j=1}^{N_{\mathrm{k}}}\sum_{i=1}^{4}\left(\overline{\boldsymbol{F}}_{\mathrm{c},i}\Delta S_i\right) \tag{21}$$

where N_{k} is the number of cells with the node k in common.

Viscous Flux Discretization. The derivative components of the viscous flux vector are approximated by assuming a constant derivative over the cell volume

$$\left(\frac{\partial u}{\partial x}\right)_j \approx \frac{1}{\Omega_j}\sum_{i=1}^{4}\left[\left(\overline{u}_{\mathrm{FA},i}\ n_{x,i}\right)\Delta S_i\right] \tag{22}$$

The derivatives required for determining the stress tensor $\overline{\boldsymbol{\tau}}$ are obtained in the same manner as the convective flux by looping over the four cell faces. As the derivative terms are piecewise constant over one cell, the surface integral of the stress tensor becomes zero. The viscous flux is, thus, computed over the supercell and the integral is discretized to give the viscous flux residual at node k

$$\boldsymbol{R}_{\mathrm{v,k}} = \oint_{\partial\Omega_{\mathrm{SC,k}}}\boldsymbol{F}_{\mathrm{v}}\,dS \approx \sum\nolimits_{i=1}^{N_{\mathrm{sub,k}}}\overline{\boldsymbol{F}}_{\mathrm{v},i}\Delta S_i \tag{23}$$

where $N_{\mathrm{sub,k}}$ is the number of faces subtending the node k and the viscous flux vector over face i is (where $\overline{\phi}_{\mathrm{CA},i}$ denotes a cell-averaged variable for a flow quantity ϕ)

$$\boldsymbol{F}_{\mathrm{v},i} \approx \begin{pmatrix} 0 \\ n_{x,i}\overline{\tau}_{xx,\mathrm{CA},j} + n_{y,i}\overline{\tau}_{xy,\mathrm{CA},j} + n_{z,i}\overline{\tau}_{xz,\mathrm{CA},j} \\ n_{x,i}\overline{\tau}_{yx,\mathrm{CA},j} + n_{y,i}\overline{\tau}_{yy,\mathrm{CA},j} + n_{z,i}\overline{\tau}_{yz,\mathrm{CA},j} \\ n_{x,i}\overline{\tau}_{zx,\mathrm{CA},j} + n_{y,i}\overline{\tau}_{zy,\mathrm{CA},j} + n_{z,i}\overline{\tau}_{zz,\mathrm{CA},j} \end{pmatrix} \tag{24}$$

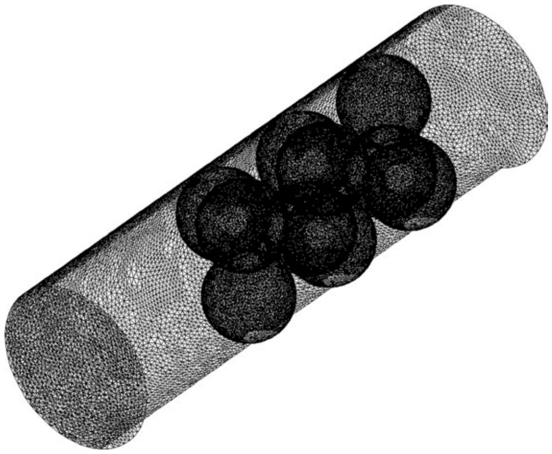

Figure 2. Wireframe outline and mesh of the packed bed geometry and volumetric mesh used in the CFD computations.

Source Terms. As the convective and viscous flux residuals are calculated over the volume of the supercells, the source terms are discretized accordingly

$$\boldsymbol{R}_{\mathrm{s,k}} = \int_{\Omega_{\mathrm{SC,k}}} \boldsymbol{Q}\, d\Omega \approx \overline{\boldsymbol{Q}_{\mathrm{k}}\, \Omega_{\mathrm{SC,k}}} \tag{25}$$

Initial and boundary conditions

Initial Conditions. Initialization of the solution is achieved by applying a constant value for velocity and pressure over the solution domain, or using the solution from a previous computation. The previous computation can be at a different mesh resolution, which facilitates the use of a coarse grid for determining the initial values on a fine mesh.

Inlet Boundary Conditions. The mass flux at the inlet is specified, along with the vector projection given in terms of the x, y, and z components of velocity.

Outlet Boundary Conditions. For a subsonic flow the outlet boundary condition is set to be the static outlet pressure, defined in this study to be atmospheric pressure. Other flow variables are extrapolated from inside the solution domain.

Wall Boundary Conditions. No-slip boundary conditions are implemented by setting all values for all the wall nodes to zero. If the energy equation is activated, the energy equation boundary equations implemented in NEWT are either a fixed wall temperature, fixed wall heat flux, or a zero temperature gradient at the wall.

Geometry and meshing

The code reads meshes generated from a suite of mesh-generation programs developed in-house.[41] It has been observed that sphere–sphere contact points may cause solution inaccuracy due to the generation of thin, unsuitable cells, or failure to generate cells at all.[32,42,43] This issue has been avoided by either under-sizing[44] or over-sizing[45] the spheres. The latter procedure is followed here, with the spheres oversized by 5%. The geometry used is shown in Figure 2. Geometric parameters of the geometry and mesh are as follows: total length, 7.07 mm; tube diameter, 2 mm; particle over-sizing, 5%; Sauter-Mean diameter, 1.2; number of spheres, 10; number of layers, 5; number of cells, 1,563,534; number of nodes, 245,047.

Table 1. Solution Parameters Chosen for the Four Computational Cases

Inlet Re_{p}	f_t	$k^{(2)}$	$k^{(4)}$	σ	C	ε_{r}
27	0.001–0.4	0.5	0.0078	0.6–0.8	2	0.3–0.5
55	0.001–0.3	0.5	0.0056–0.0078	0.6–0.8	2	0.3–0.6
111	0.001–0.2	0.5	0.0078	0.8	3	0.4–0.8
216	0.001–0.05	0.5	0.01	0.8–0.9	3	0.7–0.9

Solution strategy

The solution strategy was first to run the simulations on a coarse and intermediate grid (meshed with 367,379 and 1,021,827 cells, respectively) to provide an initial solution for the finer grid of 1,563,534 cells. The coarse grid solution was initialized with a parabolic profile condition on the assumption that the flow at the inlet is that of laminar pipe flow.

Once an initial solution was provided, the NEWT solution parameters were systematically adjusted for each case to provide the best solution convergence. The optimized parameters were selected on the basis of the evolution of the residual of axial velocity (v_x for the NEWT geometry) over a time span of 5,000 iterations from the base case. The final optimized parameters are given in Table 1. As is seen in Table 1, the value of the parameters vary depending on the state of progress of the solution. At the beginning of the solution, a small value of f_t is required to provide a stable computation, at this time the flow fields are rapidly developing. As the solution progresses, this value can be relaxed in order for a steady-state solution to be reached more quickly.

Postprocessing

Visualization and postprocessing of the results is achieved using in-house software to obtain slices through the 3-D domain and to output values of the co-ordinates and flow variables to a data file. Then, the data are imported into MATLAB and custom scripts are used to output contour plots, probability density functions (PDFs) and cumulative distribution functions (CDFs) of flow variables in addition to flow profiles over defined sections of the 2-D slice. The scripts also read in the MRI data to produce the same outputs as the CFD data. Note that in all comparisons of MRI with CFD data shown, the MRI data have been extracted from a single image; no postacquisition averaging across different datasets has been performed.

Four 1-D slices are chosen on the representative 2-D slice to validate the CFD data with the MRI data (see Figure 3).

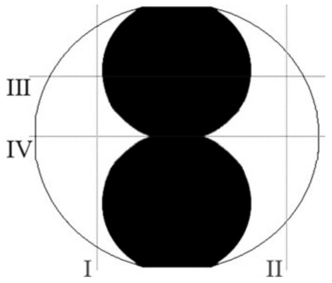

Figure 3. Representative slices of geometry chosen.

The slices through the data which are used in detailed comparisons of CFD and MRI data are identified as I-IV.

The slices parallel to the *y*-direction (I and II) are chosen to highlight the two areas in the upper and lower sections of the slice which include the velocity maxima and the edge of the computed flow field, respectively. The slices parallel to the *x*-direction (III and IV) are chosen to evaluate the area of high-flow rate in the low cross-sectional region of the bed and the region of low- and reverse-flow in the center of the bed, respectively.

The data are presented as functions of particle Reynolds number (Re_p) for the axial velocity. The notion of using the Reynolds number to compare fluid systems is consistent with the notion of dynamical similarity—the "small" CFD system uses the same Reynolds number as the "large" experimental setup to compare the two systems under the same flow conditions.[46] The Reynolds number is also correlated to the pressure drop across the bed,[47] and thus, if the average Reynolds number in the CFD simulation is different from that of the MRI data, a different pressure drop per unit length would be expected.

As the spheres for the CFD geometry are oversized, the particle Reynolds number needs to be altered. The MRI data are acquired at layers in which the free cross-sectional area is smallest, where the spheres contact the wall. This cross-sectional area is, thus, even smaller in the case of the CFD data, where the particle diameters are 5% oversized. This implies that using the same inlet condition for the MRI experiment and the CFD computation will result in a larger average flow magnitude in the CFD simulation due to the smaller cross-sectional area. The local Reynolds number for the MRI is, thus, scaled to take into account the ratio of the MRI cross-sectional area to the CFD cross-sectional by calculating the ratio between the geometry cross-sectional area and the cross-sectional area of an empty column. For a CFD grid with normal-sized spheres, this ratio is exactly 2, increasing to 2.19 for an oversizing of 5%. Therefore, the MRI Reynolds numbers are scaled by 2.19/2 to account for the oversized spheres and, hence, enable direct comparison with the CFD results.

The normalized radial distance is defined on a per-slice basis, by the length of the geometry in contact with the slice. This is to optimize use of graph space; slice III, for example, would occupy relatively little of the graph space if normalized across the same length of the geometry as slice IV.

Results and Discussion

Solution of cases

The cases were iterated to an RMS residual for axial velocity of 10^{-10}, which took between 30,000 iterations for the $Re_p = 27$ case to 50,000 iterations for the $Re_p = 55$ case. Each iteration on the fine grid took ~13 s on an Intel Xeon E5507 workstation with 12 Gb DDR3 RAM running openSUSE Linux 11.1.

Exploratory solutions on the coarse and intermediate grid were shown to be highly dependent on the nature of the flow. The inlet flows with a particle Reynolds number of 27 and 111 converged well to approximate solutions on the coarse and intermediate grids, whereas the cases with inlet particle Reynolds numbers of 55 and 216 converged less well. The fine grid solution proved to be satisfactory for the case of $Re_p = 55$. The case of $Re_p = 216$ is within the observed onset of transition to unsteady flow for this geometry, as studied by MRI,[32,48] and a fully converged solution was not achieved on either the coarse or fine grid. This could be due to the grid size not being able to resolve all of the transitioning elements of the flow field.

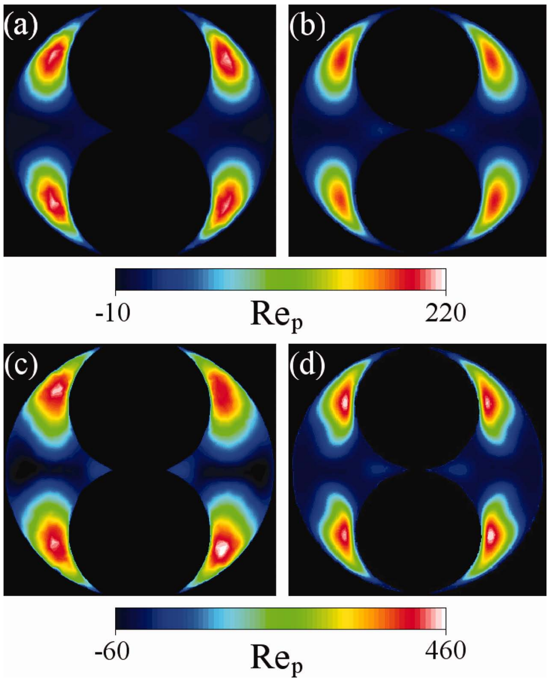

Figure 4. Filled contour plots of particle Reynolds number (based on axial velocity) for CFD and MRI flow fields.

(a) Inlet $Re_p = 27$, CFD; (b) inlet $Re_p = 27$, MRI; (c) inlet $Re_p = 55$, CFD; (d) inlet $Re_p = 55$, MRI. The 2-D datasets are obtained from the fourth particle layer from the top in the CFD simulations, and the 33rd layer from the top in the column used in the MRI experiments. [Color figure can be viewed in the online issue, which is available at wileyonlinelibrary.com.]

The cases of $Re_p = 27$, 55, and 111 are compared in detail with the MRI data; the 2-D flow maps are also shown for $Re_p = 216$ to illustrate the onset of flow instability. First, we discuss qualitatively the general form and structure of the CFD predictions compared to the MRI data. We then consider the form of the CDFs and PDFs which allows a more quantitative comparison of the accuracy of the prediction. Finally, we report the velocity profiles over the four 1-D profiles outlined in Figure 3 to investigate the flow field structures presented in the experimental and computational studies.

Flow field comparisons

Figures 4 and 5 present contour plots of particle Reynolds number based on axial velocity for the 2-D slices across the reactor geometry for $Re_p = 27$, 55, 111, and 216. The contour plots for the CFD and MRI datasets at each Reynolds number are plotted on the same absolute scale, to provide a direct and simple comparison between the CFD and MRI data.

The case of $Re_p = 27$ is presented in Figures 4a,b for the CFD and MRI data, respectively. The CFD simulation captures the tear-shaped flow pattern well, albeit with slightly higher magnitudes as seen in the center of the velocity "eyes." The central areas appear to form qualitatively the correct shape but with the CFD flow field showing greater levels of reverse flow, particularly evidenced in regions close to the wall. It is observed that there is slight asymmetry present in the MRI flow field, with the velocity eye presenting

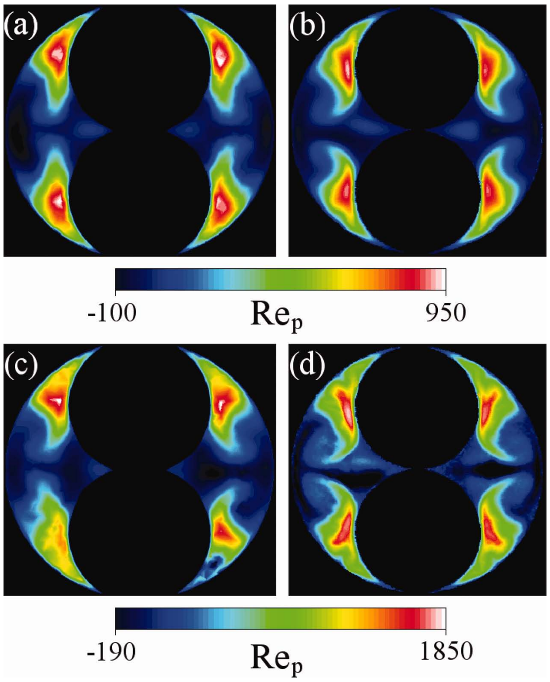

Figure 5. Filled contour plots of particle Reynolds number (based on axial velocity) for CFD and MRI flow fields.

(a) Inlet $Re_p = 111$, CFD; (b) inlet $Re_p = 111$, MRI; (c) inlet $Re_p = 216$, CFD; (d) inlet $Re_p = 216$, MRI. The 2-D slices are obtained from the same slices in the simulations and experiment as those shown in Figure 4. [Color figure can be viewed in the online issue, which is available at wileyonlinelibrary.com.]

slightly higher magnitudes in the lower-right and upper-left regions. This is most likely due to the slightly imperfect packing of the real column—even if the layer at which the data were acquired was packed perfectly, previous imperfectly packed layers would still impact the flow field further down the column.

The case of $Re_p = 55$ is presented in Figures 4c,d for the CFD and MRI data, respectively. At this Reynolds number, a concave curvature is manifested at the edge of the velocity eye regions in the MRI results. This is also captured in the CFD simulation but not to the same extent as in the MRI image. It is possible that the choice of numerical parameters required to ensure stability has restricted the extent of the realization of the curvature in the flow field. Higher reverse flow is also observed in the central region of the CFD image and a slight asymmetry is present across the velocity eyes. The computed flow field in this case is satisfactory—the main elements of the flow have been captured.

The case of $Re_p = 111$ is presented in Figures 5a,b for the CFD and MRI data, respectively. At this higher particle Reynolds number, the velocity eyes present a concave form with more extreme curvature. Asymmetry is observed again in the MRI data. The CFD simulation here appears to capture the key flow elements with the correct magnitude. The velocity eyes do not exhibit the same degree of curvature as presented in the MRI data and the central portion of the high velocity region is slightly more rounded in contrast to the longer auriform flow in the MRI image. The negative flow to the side of the central region is again overemphasized in the CFD prediction.

The highest flow case of $Re_p = 216$ is presented in Figures 5c,d for the CFD and MRI data, respectively. This case was the most difficult case to converge, presumably due to the onset of transition and consequently the need for a finer grid to resolve the fine flow structures. Following on from the previous cases, the velocity eye again contracts longitudinally and further curvature of the velocity eye is observed, with some flow detachment around the curvature. There is evidence of some unsteadiness in the flow, particularly in the bottom half of the flow field. However, the quantitative comparison is relatively good, capturing the same range of particle Reynolds numbers across the geometry. The unsteadiness could potentially be resolved with a finer mesh; the bottom-left velocity eye in the CFD image appears to be resolving itself into the shape displayed in the MRI image, but the solution was not developing quickly. This could be due to more restrictive solution controls required in regions of high-velocity gradients such as around the eye, or the need to be able to vary the numerical parameters across different regions of the mesh.

Velocity distributions

The CDFs shown in Figure 6 present the distribution of particle Reynolds numbers in the representative 2-D slices. This allows a comparison between the CFD and the MRI data by plotting the fraction of the flow having a magnitude of a certain value or lower. The PDFs shown in Figure 6 indicate the probability of finding a certain value of Re_p within the flow, giving a quantitative measure of the dominating features within the flow.

For the case of $Re_p = 27$, the CDF of the CFD case (dashed line) matches the distribution of the MRI data (black solid line) very well (see Figure 6a). There is a slight systematic overprediction by the CFD computation up to a Reynolds number of ~150, but the MRI data approaches the limiting value of unity before the CFD data. This implies an overprediction by the computation of the high-velocity flow fields near to the particles. The MRI CDF also approaches zero before the CFD CDF does, again implying an overprediction of the reverse-flow near to the center of the geometry. This could be due to a number of factors—grid fineness and the representative geometry (not enough layers for a fully developed flow) are two possible causes. The two PDFs for this case (Figure 7a) are also in good agreement and reinforce what is seen in the CDF—an over-prediction of the high and low Reynolds numbers, particularly around the point of zero flow. As the flow is laminar, a large stagnant region is expected given the relatively stable nature of the flow and the effect of the geometry. The relative median error (with reference to the MRI data) in the flow field for the case of $Re_p = 27$ curve is 4%, demonstrating excellent agreement with the MRI data. This error is calculated only from the difference between the computed CFD and measured MRI values and does not include experimental error.

The case of $Re_p = 55$ (Figure 6b) presents the least satisfactory prediction for the CDF but overall there is good agreement. The two distributions converge at high Reynolds numbers, indicating that the central velocity "eye" has been correctly predicted. The simulation tends to overpredict reverse flow at the center of the geometry but gives a relatively smooth quantitative flow distribution. The PDF for this case (Figure 7b) is of interest as the peak for the MRI data for zero-flow is higher than the CFD value, implying a

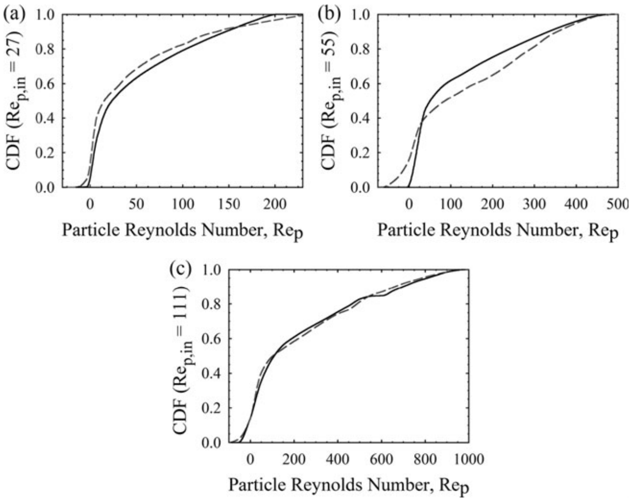

Figure 6. CDFs of particle Reynolds number over the representative 2-D slices.

The CFD and the MRI data are shown by the dashed and solid lines, respectively. Data are shown for inlet flows of (a) $Re_p = 27$, (b) $Re_p = 55$ and (c) $Re_p = 111$.

greater distribution of stagnant flow than that is predicted by the computational model (the reverse is true for the other cases). These inaccuracies are reflected in the median error of the computational result of 9%. Future work will involve exploring this result in more detail.

The case of $Re_p = 111$ (Figure 6c) also predicts the quantitative flow distribution very well, with a median relative error of 2.8%. The MRI flow field shows maldistribution of the flow at a Reynolds number of ~600—this could be due to the nonideal packing in the reactor or the imaging of a nonsteady state in the reactor. The PDF for this case (Figure 7c) shows that the CFD simulation contains fluctuations at intermediate Reynolds numbers. This could be as a result of an incompletely converged solution or an issue with computational grid resolution as was shown by the case of $Re_p = 216$ in Figure 5c, indicating that more refined meshes are required to capture the onset of transition and the finer curvature of the flow field.

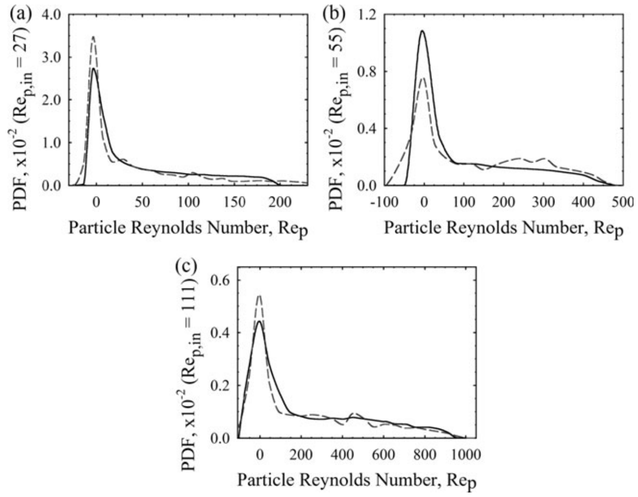

Figure 7. PDFs of particle Reynolds number over the representative 2-D slices.

The CFD and the MRI data are shown by the dashed and solid lines, respectively. Data are shown for inlet flows of (a) $Re_p = 27$, (b) $Re_p = 55$ and (c) $Re_p = 111$.

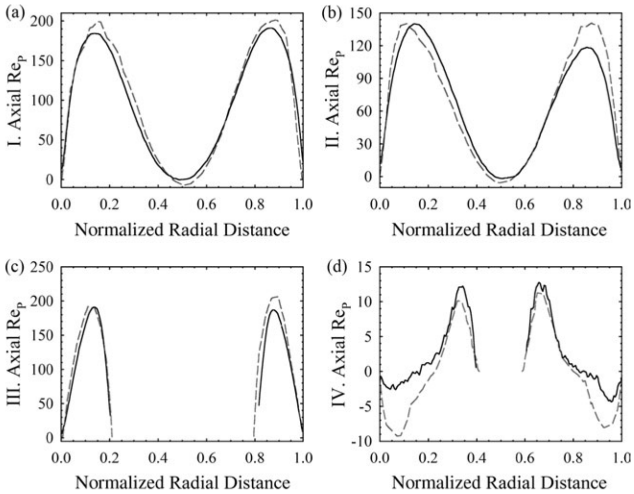

Figure 8. Particle Reynolds number as a function of normalized radial distance for inlet $Re_p = 27$, over the four slices through the 2-D datasets identified in Figure 3.

The CFD and the MRI data are shown by the dashed and solid lines, respectively.

Velocity profiles

To provide a more detailed quantitative assessment and validation of the CFD code, four 1-D slices were taken over each 2-D slice, as identified in Figure 3. These slices have been chosen to investigate the major flow field structures in each case—the velocity eyes, and the distribution of stagnant and reverse flow around the center of the geometry. Figures 8–10 show a comparison of the CFD- and MRI-derived axial values of Re_p for each of the four slices, for inlet particle Reynolds numbers of 27, 55, and 111, respectively. The CFD and MRI data are shown by the dashed and solid lines, respectively.

Figure 8 presents the 1-D slices for the case of $Re_p = 27$, which has already been shown to give good agreement of the CFD with the MRI data, albeit with slight overprediction of the velocity eyes and the central flow. This is also

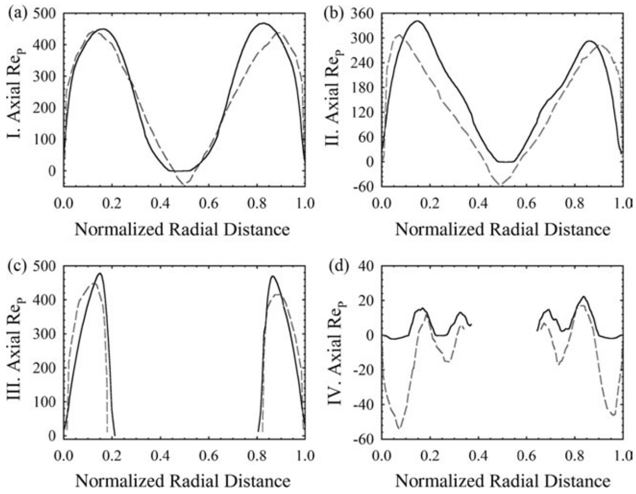

Figure 9. Particle Reynolds number as a function of normalized radial distance for inlet $Re_p = 55$, over the four slices through the 2-D datasets identified in Figure 3.

The CFD and the MRI data are shown by the dashed and solid lines, respectively.

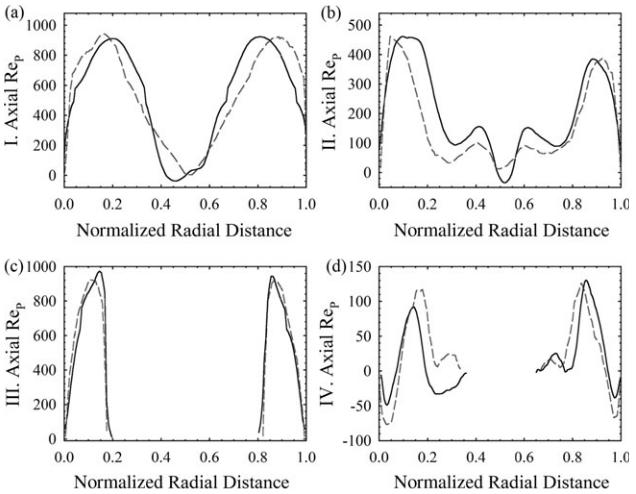

Figure 10. Particle Reynolds number as a function of normalized radial distance for inlet Re_p = 111, over the four slices through the 2-D datasets identified in Figure 3.

The CFD and the MRI data are shown by the dashed and solid lines, respectively.

evidenced in the 1-D slices; slices I and III yield higher peaks of Re_p than those in the MRI data. The difference is small, in the region of ~10% for slice I. Slice III shows the asymmetry present in the MRI data, and more surprisingly also for the CFD case. The asymmetry in the MRI data is also shown in slice II, representing the edge of one of the velocity eyes. The peaks in the CFD solution are translated toward the walls of the geometry, demonstrating a higher-velocity gradient near to the walls than that was observed in the MRI data. The central slice (IV) shows the increased negative flow for the CFD cases. The asymmetry in the MRI data results in the minimum being present on one side of the curve. Although the magnitude of the negative flow is overpredicted, the flow field pattern appears to be correct. The CFD again shows a greater velocity gradient closer to the wall than the MRI data. This could be as a result of the no-slip boundary implemented by the CFD code, enforcing zero velocity at the wall but not stipulating the allowable gradients in nodes near to the boundary. An alternative reason is the oversized spheres causing the shift in the normalized radial position.

Figure 9 presents the 1-D slices for the case of $Re_p = 55$. The earlier analysis showed that the CFD prediction for this case gave a greater concentration of stagnant flow and less reverse flow in the MRI flow field, with both flow fields showing approximately the same maximum value for Re_p. Slice I yields similar curves for the two data sets, with the CFD computation having a more well-defined minimum. The MRI data here approach zero-flow in between the two velocity eyes, as evidenced in the PDF in Figure 7b by the peak around the point $Re_p = 0$. Slice III shows the 1-D slice across the top two velocity eyes, showing the numerical discrepancy of the right-hand eye as previously observed in the contour plot of Figure 4c. This discrepancy could be due to the solution parameters being too relaxed in the final computations. Slice IV across the center further demonstrates the overprediction of reverse flow by the CFD simulation. The qualitative flow field representation in this region is good, with both of the twin peak shapes accurately conveyed for the CFD flow field but with the representative minima being smaller than expected. The existence of the twin peaks could be due to the dual interactions of the flow with the high-velocity fields at the top and bottom of the domain and the sphere contact point. The peaks due to particle contact would be expected to be more dominant in the CFD simulation than the MRI data (as shown in slice IV) due to the oversized spheres in the CFD geometry giving a larger liquid–solid contact surface area.

Figure 10 shows the representative slices for $Re_p = 111$. This case showed excellent agreement of the PDF between the CFD and the MRI, and good qualitative agreement in the flow field comparison. Here, the velocity eyes predicted by the CFD (slices I and III) show excellent quantitative agreement, with the CFD peaks occurring closer to the wall as previously witnessed. It is interesting to note that a point of inflexion is observed in the MRI data after the central minimum. This could be due to the interaction of the reverse flow nearby with the low velocity flow at the end of the curvature in the eye. Slice II shows the velocity distributions at the edge of the eye on the right-hand side of the particle, with the CFD simulation capturing the shape of the flow field very well. The CFD velocity gradient is higher closer to the wall and the central three local extrema are smaller in magnitude than the MRI data. The magnitude of the peaks here is relative to the amount of curvature at the edge of the eye; the 1-D slice passes through the edge of the eye and, thus, bisects each eye twice, once in the "bulk" and once in the curvature. Thus, a larger degree of curvature would lead to a lower minimum point due to a larger reverse-flow region encapsulated by the curve, as is observed in the contour plots in Figures 5a,b. If the CFD solution was allowed to converge further to a more curved solution, the minimum of the curve might approach that of the MRI curve. The central flow profile in slice IV yields the distinctive two peaks seen for the previous case, with larger outer peaks as expected due to the increased contact of the two high-velocity regions for this case. The MRI data here exhibit the reverse flow before the wall that the CFD computations also suggest, perhaps indicating the onset of the transition regime and a more unsteady flow.

Conclusions

This article has presented direct validation of a single-phase CFD code (NEWT) using MRI data for a packed bed with a particle-to-column diameter of two. The agreement between computational and experimental flow fields is generally very good, and serves to increase confidence in the use of CFD as a modeling tool for predicting flow fields at low Reynolds number in packed-bed reactors with complex pore spaces. This method of validation is essential for ensuring accurate design and optimization work—validations based on global hydrodynamical parameters give no basis for the accuracy of the flow fields computed within the geometry, which are essential for design and scale-up of processes. The errors in the computational data were shown to be 4, 9, and 2.8% for the cases of Re_p = 27, 55, and 111, respectively, demonstrating excellent agreement with the MRI data.

Several interesting flow features were noted. First, CFD tends to overpredict the amount of reverse flow in the center of the geometry. This could be due to the relatively small representative length of the reactor chosen in the CFD modeling (five layers, as opposed to 69 in the MRI experiment), thus, not allowing the velocity components to approach a fully steady-state solution. Second, the CFD systematically predicts the velocity peaks as being closer to the wall. This could be as a result of the strict implementation of the no-slip conditions at the wall leading to higher-velocity gradients or more simply due to the slight oversizing of the particle artificially shifting the position at which these peaks in velocity occur. Third, the slice over the center of the geometry showed the existence of two peaks; these were explained as resulting from the interaction of the flow with the wall and the particle contact points. The peaks representative of the wall–fluid contact had larger maxima than the particle–fluid contact peak, and the particle–fluid contact peaks were more evident for the CFD flow fields due to the slight oversizing of the particles, leading to greater surface interactions with the fluid. Finally, as the inlet particle Reynolds number increases, the flow becomes more concave and forms strong curvature at the base of each of the high-velocity regions. This is reflected in the velocity slices by the existence of a minimum point in between two local maxima. The CFD code under-predicted the magnitude of curvature in comparison to the MRI data, possibly due to the solution not being fully iterated to steady-state. A further 10,000 iterations (taking approximately one and a half days) yielded only a small increase in the magnitude of curvature, therefore, further increasing the number of iterations was not considered. Relaxation of the numerical parameters for faster convergence is not always possible due to the need for the flow to converge in a stable manner.

This work has also served to validate preconditioning as a tool to solve for pressure within low Mach number systems, allowing numerical methods developed for compressible solvers to be used for incompressible flow. The important advantage of preconditioning is the ability to retain solution stability when solving for compressible flow at low Mach numbers—this will be important in cases where density fluctuations occur in a low Mach number flow, such as in strongly exothermic and endothermic reactive flows in packed beds. For this case, MRI is seen as an important tool for validation of CFD due to its ability to measure noninvasively at high spatial resolution a wide variety of local flow quantities. It is expected that the strategy of validation of CFD codes with MRI data will allow increasing validation of more complex flow regimes such as the transition regime, turbulence, and two-phase flow. The validated NEWT code serves as a computational foundation on which more interesting flows can now be computed. Future work will aim to investigate the implementation of reaction and two-phase flow into NEWT, and validation of the CFD computation with further MRI and reaction data. The validation of the preconditioning method for single-phase flow creates a foundation on which two-phase flow studies at low Mach numbers can be investigated. The impact of numerical parameters and the mesh on solution stability and accuracy will also be investigated.

Acknowledgments

This work was funded under the CASTech project (EPSRC reference EP/G011397/1); EPSRC and Johnson Matthey are thanked for financial support. The authors gratefully acknowledge Prof. Bill Dawes and Cambridge Flow Solutions for the NEWT source code, and Dr. Andy Sederman for help with the processing of the MRI data. Sunday Omowunmi and Dr. Caleb Dhanasekaran are gratefully acknowledged for the geometry and mesh which were used in this study.

Notation

C = Coefficient for time step calculation

$\boldsymbol{F}_c$ = Convective flux vector

$\boldsymbol{F}_v$ = viscous flux vector

$\boldsymbol{K},\boldsymbol{K}^{-1}$ = transformation and inverse transformation matrix

N = column-to-particle diameter ratio

N_k = number of nodes neighboring node k

Pr = fluid Prandtl number

$\boldsymbol{Q}$ = source term vector

$\boldsymbol{R}_{tot,k}$ = sum of viscous flux $\boldsymbol{R}_{v,k}$, convective flux $\boldsymbol{R}_{c,k}$, source term $\boldsymbol{R}_{s,k}$ and artificial dissipation $\boldsymbol{R}_{AD,k}$ residuals

$\boldsymbol{R}^*$ = smoothed residual

Re_p = particle Reynolds number (dimensionless)

U_r = reference velocity term, m s^{-1}

V = contravariant velocity, $V \equiv v \cdot n$ (V^{-1}—modified for preconditioned system), m s^{-1}

$\boldsymbol{W}$ = conservative variable vector

$\boldsymbol{W}_p$ = primitive variable vector

c = speed of sound (c' – modified for preconditioned system), m s^{-1}

d_p = particle diameter, m

d_t = tube diameter, m

$f_{e,i}$ = i component of body forces (gravity, buoyancy, etc.) per unit mass

f_t = NEWT time step factor

$\boldsymbol{n}$ = surface normal vector

n_i = component of surface normal vector in i direction

p_i = absolute pressure, ith component, Pa

u,v,w = x-, y- and z- components of velocity, m s^{-1}

$\boldsymbol{\Gamma},\boldsymbol{\Gamma}_{nc}$ = Conservative/nonconservative preconditioning matrix

Δh = Measure of the CFD cell size, m

Δt = Solution time step, s

θ = Preconditioning parameter

$\overline{\phi}_{CA,j}$ = Generic flow quantity ϕ averaged over cell j

$\overline{\phi}_{FA,i}$ = Generic flow quantity ϕ averaged over face i

Ω = CFD cell volume, m^3

Ω_{SC} = CFD supercell volume, m^3

α_m = Runge-Kutta stage coefficient, stage m

ε = Arbitrary small number for reference velocity definition (NEWT: 10^{-3})

ε_r = Residual smoothing coefficient

κ = Thermal diffusivity of fluid, m^2 s^{-1}

μ = Dynamic viscosity, Ns m^{-2}

v = Kinematic viscosity, m^2 s^{-1}

ρ = Fluid density, kg/m^3

σ = Courant number

σ_{ij} = ijth component of viscous stress tensor

Literature Cited

1. Al-Dahhan MH, Larachi F, Dudukovic MP, Laurent A. High-pressure trickle-bed reactors: a review. *Ind Eng Chem Res.* 1997;36: 3292–3314.
2. Hekmat D, Feuchtinger A, Stephan M, Vortmeyer D. Microbial composition and structure of a multispecies biofilm from a trickle-bed reactor used for the removal of volatile aromatic hydrocarbons from a waste gas. *J Chem Technol Biotechnol.* 2004;79:13–21.
3. Satterfield CN. Trickle-bed reactors. *AIChE J.* 1975;21:209–228.
4. Anadon LD, Sederman AJ, Gladden LF. Mechanism of the trickle-to-pulse flow transition in fixed-bed reactors. *AIChE J.* 2006;52: 1522–1532.
5. Holub RA, Dudukovic MP, Ramachandran PA. Pressure drop, liquid holdup and flow regime transition in trickle flow. *AIChE J.* 1993;39: 302–321.
6. Iliuta I, Ortiz-Arroyo A, Larachi F, Grandjean BPA, Wild G. Hydrodynamics and mass transfer in trickle bed reactors: an overview. *Chem Eng Sci.* 1999;54:5329–5337.
7. Specchia V, Baldi G. Pressure drop and liquid holdup for two phase concurrent flow in packed beds. *Chem Eng Sci.* 1977;32:515–523.
8. Blok JG, Varkevisser J, Drikenburg AAH. Transition to pulsing flow, holdup and pressure drop in packed columns with cocurrent gas-liquid downflow. *Chem Eng Sci.* 1983;38:687–699.
9. Dankworth DC, Kevrekidis IG, Sundaresan S. Dynamics of pulsing flow in trickle beds. *AIChE J.* 1990;36:605–621.
10. Larachi F, Iliuta I, Chen M, Grandjean BPA. Onset of pulsing in trickle beds: evaluation of current tools and state-of-the-art correlation. *Can J Chem Eng.* 1999;77:751–758.
11. Ng KM. A model for flow regime transitions in cocurrent downflow trickle-bed reactors. *AIChE J.* 1986;32:115–122.
12. Saroha AK, Nigam KDP. Trickle bed reactors. *Rev Chem Eng.* 1996;12:207–347.

13. Gunjal PR, Madhavanand NK, Ranade VV, Chaudhari RV. Hydrodynamics of trickle-bed reactors: experiments and CFD modeling. *Ind Eng Chem Res.* 2005;44:6278–6294.
14. Brandvik T, Pullan G. Acceleration of a 3D Euler solver using commodity graphics hardware. 46th AIAA Aerospace Sciences Meeting, Reno, NV, 2008.
15. Brandvik T, Pullan G. An accelerated 3D Navier-Stokes solver for flows in turbomachines. *Proceedings of GT2009 ASME Turbo Expo 2009*. Orlando, FL, 2009.
16. Elsen E, LeGresley P, Darve E. Large calculation of the flow over a hypersonic vehicle using a GPU. *J Comput Phys.* 2008;227: 10148–10161.
17. Harris MJ, Baxter III WV, Scheuermann T, Castra A. Simulation of Cloud Dynamics on Graphics Hardware. In: *Proceedings of the 2003 ACM SIGGRAPH/EUROGRAPHICS Conference on Graphics Hardware*, pp. 92–101. San Diego, CA, 2003.
18. Gunjal PR, Ranade VV, Chaudhari RV. Computational study of a single-phase flow in packed beds of spheres. *AIChE J.* 2005;51: 365–378.
19. Suekane T, Yokouchi Y, Hirai S. Inertial flow structures in a simple-packed bed of spheres. *AIChE J.* 2003;49:10–17.
20. Weiss J, Smith WA. Preconditioning applied to variable and constant density flows. *AIAA J.* 1995;33:2050–2057.
21. Jiang Y, Khadilkar MR, Al-Dahhan MH, Dudukovic MP. CFD of multiphase flow in packed-bed reactors. 1. k-fluid modeling issues. *AIChE J.* 2002;42:701–715.
22. Jiang Y, Guo J, Al-Dahhan MH. Multiphase flow packed-bed reactor modeling: combining CFD and cell network model. *Ind Eng Chem Res.* 2005;44:4940–4948.
23. Lopes RJG, Quinta-Ferreira RM. CFD modelling of multiphase flow distribution in trickle beds. *Chem Eng J.* 2009;147:342–355.
24. Lappalainen K, Manninen M, Alopaeus V. CFD modeling of radial spreading of flow in trickle-bed reactors due to mechanical and capillary dispersion. *Chem Eng Sci.* 2009;64:207–218.
25. Bai H, Theuerkauf J, Gillis P, Witt PM. A coupled DEM and CFD simulation of flow field and pressure drop in fixed bed reactor with randomly packed catalyst particles. *Ind Eng Chem Res.* 2009;48: 4060–4074.
26. Dixon AG, Nijemeisland M. CFD as a design tool for fixed-bed reactors. *Ind Eng Chem Res.* 2001;40:5246–5254.
27. Dixon AG, Nijemeisland M, Stitt EH. CFD simulation of reaction and heat transfer near the wall of a fixed bed. *Int J Chem React Eng.* 2003;A2:1–18.
28. Dixon AG, Taskin ME, Stitt EH, Nijemeisland M. 3D CFD simulations of steam reforming with resolved intraparticle reaction and gradients. *Chem Eng Sci.* 2007;62:4963–4966.
29. Sederman AJ, Johns ML, Bramley AS, Alexander P, Gladden LF. Magnetic resonance imaging of liquid flow and pore structure within packed beds. *Chem Eng Sci.* 1997;52:2239–2250.
30. Sederman AJ, Johns ML, Alexander P, Gladden LF. Structure-flow correlations in packed beds. *Chem Eng Sci.* 1998;53:2117–2128.
31. Sederman AJ, Gladden LF. Magnetic resonance imaging as a quantitative probe of gas–liquid distribution and wetting efficiency in trickle-bed reactors. *Chem Eng Sci.* 2001;56:2615–2628.
32. Sains MC. Ultra-fast visualisation of unsteady flow using magnetic resonance imaging. Unpublished doctoral dissertation. University of Cambridge, UK, 2006.
33. Sains MC, El-Bachir MS, Sederman AJ, Gladden LF. Rapid imaging of fluid flow patterns in a narrow packed bed using MRI. *Mag Res Imag.* 2005;23:391–393.
34. Dawes WN. The development of a solution-adaptive 3D Navier-Stokes solver for turbomachinery. *27th AIAA/SAE/ASME/ASEE Joint Propulsion Conference*. Sacramento, CA, 1991.
35. Volpe G. Performance of compressible flow codes at low Mach number. *AIAA J.* 1993;31:49–56.
36. Cabuk H, Sung CH, Modi V. Dimensional internal incompressible flows. *AIAA J.* 1992;30:2024–2031.
37. Blazek J. *Computational Fluid Dynamics: Principles and Applications*, 1st ed. Oxford: Elsevier Science, 2001.
38. Chorin AJ. A numerical method for solving incompressible viscous flow problems. *J Comp Phys.* 1997;135:118–125.
39. Dawes WN. The simulation of three-dimensional viscous flow in turbomachinery geometries using a solution-adaptive unstructured mesh methodology. *Trans ASME.* 1992;114:3–50.
40. Hall MG. Cell-vertex multigrid scheme for solution of the Euler equations. In: *Proceedings of the International Conference on Numerical Methods for Fluid Dynamics*. Reading, UK, 1985.
41. Dawes WN, Dhanasekaran PC, Demargne AAJ, Kellar WP, Savill AM. Reducing bottlenecks in the CAD-to-mesh-to-solution cycle time to allow CFD to participate in design. *Trans ASME.* 2001;123: 552–557.
42. Logtenberg SA, Nijemeisland M, Dixon AG. Computational fluid dynamics simulations of fluid flow and heat transfer at the wall particle contact points in a fixed bed reactor. *Chem Eng Sci.* 1999;54: 2433–2439.
43. Lopes RJG, Quinta-Ferreira RM. Three-dimensional numerical simulation of pressure drop and liquid holdup for high-pressure trickle bed reactor. *Chem Eng J.* 2008;145:112–120.
44. Nijemeisland M, Dixon AG. Comparison of CFD simulations to experiment for convective heat transfer in a gas-solid fixed bed. *Chem Eng J.* 2001;82:231–246.
45. Guardo A, Coussirat M, Larrayoz MA, Recasens F, Egusquiza E. CFD flow and heat transfer in nonregular packings for fixed bed equipment design. *Ind Eng Chem Res.* 2004;43:7049–7056.
46. Duckler AE, Wicks III M, Cleveland RG. Frictional pressure drop in two-phase flow: B. An approach through similarity analysis. *AIChE J.* 1964;10:44–51.
47. Ergun S, Orning AA. Fluid flow through randomly packed columns and fluidized beds. *Ind Eng Chem.* 1949;41:1179–1184.
48. El-Bachir MS. MRI study of flow in narrow packed beds. Unpublished doctoral dissertation. University of Cambridge, UK, 2005.

Manuscript received Aug. 11, 2011, revision received Jan. 13, 2012.